THE JOURNAL OF PHYSICAL CHEMISTRY LETTERS
A JOURNAL OF THE AMERICAN CHEMICAL SOCIETY

pubs.acs.org/JPCL

Letter

Unveiling the Mechanism of Negative Poisson's Ratio in Phosphorus-like 2D MX Materials Driven by Geometric and Electronic Structures

Yahong Pu, Jie Zhang, Peixuan Li, Guolin Wan, Jinbo Pan, Yan-Fang Zhang,* and Shixuan Du*

Cite This: *J. Phys. Chem. Lett.* 2025, 16, 5820−5826

Read Online

ACCESS | Metrics & More | Article Recommendations | Supporting Information

ABSTRACT: Two-dimensional black-phosphorus-like materials with a re-entrant structure have been reported exhibiting positive or negative Poisson's ratio (NPR). However, uncovering the underlying geometric−electronic interplay and identifying design principles for NPR materials remain challenging. Using first-principles calculations, we investigate 26 two-dimensional black-phosphorus-like MX monolayers with 10 valence electrons (M = cation, X = anion). Among them, PN, AsN, SbN, AsP, and GeSe exhibit out-of-plane NPR. Geometric structure analysis using machine learning links NPR to the variation of the X−M−X bond angle (θ_M) and M−X−X−X dihedral angle (φ). Under zigzag (y)-direction strain, a larger reduction in θ_M and a greater increase in φ are more favorable for NPR formation. Electronic structure analysis attributes the out-of-plane NPR under y-axis strain to the cation−anion p_z orbital interaction. For NPR materials with the same X element, a higher atomic number of M corresponds to a more negative Poisson's ratio. This work advances the development of novel materials with unique mechanical behaviors.

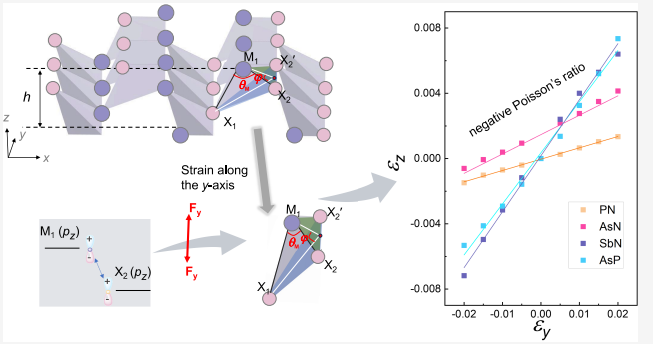

Negative Poisson's ratio (NPR) is an auxetic mechanical property[1] characterized by a transverse expansion/contraction in a material under vertical tensile/compressive strain.[2] The unique phenomenon enhance the toughness,[3−5] shear strength,[6−9] energy absorption characteristics,[10−13] effective sound/vibration absorption,[11,13] and so on. Consequently, NPR materials hold promise for applications in mechanical engineering and micro/nanoelectronics devices. Research studies on NPR have expanded from traditional artificial structures[14−17] to the realm of two-dimensional (2D) materials,[18−25] including the transition metal chalcogenides MX_2[26] and M_2X_3 (M = Ni, Pd, X= S, Se, Te),[27] wurtzite monolayers,[22] Pd-decorated borophene,[28] single-layer MoS_2,[29] and so on.[30−32] The NPR effect was initially attributed solely to geometric structures, such as re-entrant structures,[33−35] flexible hinges,[36,37] and star-shaped structures.[38] Recent research reported that the auxetic effect in group-VI 1T-type monolayer transition metal dichalcogenides (TMDs) is related to the d-electron count.[39] Yu et al. demonstrated that the NPR of R-Cu_2Se_2 monolayer can be attributed to the lone-pair electrons and weak electronegativity of Se atoms.[23] Later, Pan et al. proposed that the auxetic mechanical behavior in 2D transition metal selenides and halides originates from the electronic structure.[40] These studies highlight the role of the electronic structure in auxetic behavior, as exemplified by recent advances.[23,41]

However, the influence of the interplay between the electronic structure and geometry on Poisson's ratio is intricate. For example, despite the same valence electrons and geometric configurations of 2D NiX_2 (X = S, Se, Te), only $NiTe_2$ exhibits auxetic behavior.[42] In another case, while the 2D black phosphorus (α-phosphorene) monolayer is recognized as an NPR material,[36] its isostructural counterparts, SnS, SnSe, and GeS, exhibit NPR characteristics under strain along the armchair direction. In contrast, GeSe exhibits positive Poisson's ratio characteristics. Therefore, the physical origin of the NPR in these 2D materials is important for the design of materials with similar structures and for their further applications. Recently, Liu et al. identified a family of black phosphorus-like structures 2D materials. These black phosphorus-like 2D materials, which possess ten valence electrons with similar geometric structures, provide a platform to investigate the roles of the electronic structures and geometry factors in the intricate NPR phenomenon.

Received: May 7, 2025
Revised: May 27, 2025
Accepted: May 29, 2025
Published: June 4, 2025

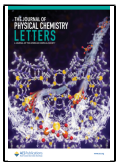

https://doi.org/10.1021/acs.jpclett.5c01362
J. Phys. Chem. Lett. 2025, 16, 5820−5826

In this work, using density functional theory (DFT) based calculations, we investigated the mechanical characteristics of 26 black phosphorus-like 2D materials (MX) with 10 valence electrons. Under strain along the zigzag (y) direction, five NPR materials are identified: PN, AsN, SbN, SbP, and GeSe. By applying a machine learning random forest model, we found that the variations in the bond angle of X−M−X (θ_M) and the dihedral angle of M−X−X−X (φ) are critical in determining Poisson's ratios. Specifically, a greater strain-induced reduction in θ_M and an increase in φ are more conducive to NPR formation, which is further validated by 2D black phosphorus. Electronically, the out-of-plane NPR under y-axis strain is attributed to the interaction between the p_z orbitals of the M and X atoms. Additionally, we establish a correlation among the elemental composition, structural parameters, and NPR values. For NPR materials with the same anion element X, a higher atomic number of M typically leads to a more negative Poisson's ratio. These findings reveal that the formation of NPR in 2D black phosphorus-like systems is induced by a combination of geometric configurations and electric structures, offering a valuable framework for the future design of functional materials.

Poisson's Ratio of MX Materials. A puckered structure prototype based on 2D black phosphorus is used as a basis for the exploration of 26 distinct 2D MX materials, where M represents the cation and X represents the anion. All materials possess ten valence electrons and exhibit high stability. To fulfill the condition of ten valence electrons, the elements M (X) originate from either group III or IV (VII or VI), or both from group V. As illustrated in Figure 1(a), M serves as a cation within the purple-shaded region, whereas X denotes an anion within the pink-shaded region. Figure 1(b) presents the top and side views of the puckered structure, exhibiting distinct characteristics along the x (armchair) and y (zigzag) directions.

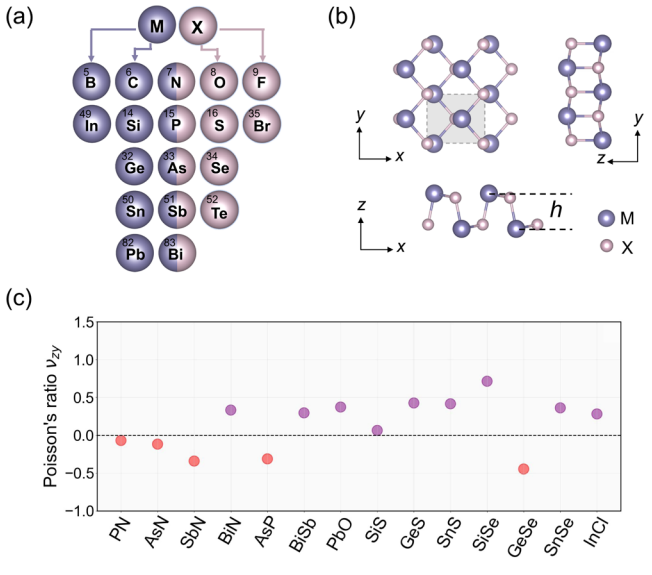

Figure 1. Compositions, configurations, and Poisson's ratio of 2D black phosphorus-like materials. (a) The binary MX systems, composed of a purple-shaded M atom and a pink-shaded X atom. (b) Top and side views of the structures. The gray rectangle represents the primitive cell. The h is the vertical distance between the upmost and the bottom atomic layers. (c) Poisson's ratio under strain along the y-direction. The positive and negative Poisson's ratios are colored in purple and pink spots, respectively.

The thickness of these monolayers, denoted as h, is defined as the vertical distance between the top and bottom atomic layers.

The in-plane and out-of-plane Poisson's ratios are investigated under uniaxial strain from −2% to 2% along the x- and y-directions, respectively. The detailed calculation results of Poisson's ratio are summarized in the Table S1. Materials failing to maintain linear strain response within the −2% to 2% range are excluded from the discussion. The out-of-plane NPR (υ_{zx}) of materials such as SiS, SiSe, GeS, SnS, and SnSe has been well discussed in previous studies[44] when strain is applied along the x-directions. Here, we mainly focus on the mechanism of NPR materials under y-axis strains. Figure 1(c) shows Poisson's ratio υ_{zy} under the y-axis strains. Among the 26 materials, PN, AsN, AsP, SbN, and GeSe exhibit out-of-plane NPR characteristics. Figure S1 shows the fitting curves of the representative NPR materials.

To evaluate the potential influence of spin−orbit coupling (SOC), we calculated the Poisson's ratios of selected materials with SOC included. The results show that SOC induces negligible changes in both the lattice constants and the NPR values, confirming its limited impact on the mechanical response in this work (Figures S3 and S4 and Table S2).

Geometric Structure Effects on the Poisson's Ratio. The influence of the geometric structure on Poisson's ratio was explored. The bond lengths and bond angles in the geometric structure intuitively correspond to the parameter h, which is the vertical distance between the top and bottom atomic layers. Under a y-axis tensile strain, the negative value of the Poisson's ratio in the z-direction is related to an increase in h in the linear range. The change in h, Δh, can be expressed as $\Delta h = h' - h_0$ (h' and h_0 represent the vertical distance at a 2% tensile strain and without strain, respectively). The top figure in Figure 2(a) is the side view of the geometric structure marked with the bond lengths (d_1, d_2), bond angles (θ_M, θ_X, θ) and dihedral angle φ. Thus, Δh is further explored by performing a mathematical derivation with consideration of bond lengths and bond angles. The detailed mathematical derivation is detailed in the Supporting Information (SI). All parameters remain in the final equation, indicating that the influence of each parameter on Δh is irreplaceable and that all the structural parameters contribute to the Poisson's ratio. Figure 2(b) presents the relation of the Poisson's ratio and Δh. The Poisson's ratio is negative for the materials in the pink shaded area, corresponding to an increase of h, that is, Δh is positive.

Next, since Δh is related to d_1, d_2, θ_M, θ_X, θ, and φ, a machine learning random forest model is employed to further identify the primary factors and thus assess their impact on Poisson's ratio. Each material is characterized by six features (variations in the above parameters) and a label Δh. The data set is divided into a training set and a test set in a 4:1 ratio. As shown in Figure 2(c), the training results reveal that the weights of the parameters Δd_1, Δd_2, $\Delta\theta_M$, $\Delta\theta_X$, $\Delta\theta$, and $\Delta\varphi$ are 0.10, 0.08, 0.09, 0.27, 0.15, and 0.30, respectively. Figure S6 shows the Δh values calculated by DFT and those predicted by machine learning. The scatters demonstrate a positive correlation, thereby validating the accuracy of the model. Thus, the variations of bond angle θ_M and dihedral angle φ play an important role in the positive and negative Poisson's ratio, while the impact of the bond length is relatively minor.

Figure 2(d) illustrates the relationships between υ_{zy} and $\Delta\theta_M$, $\Delta\varphi$, showing a relatively linear correlation. The results indicate that a greater decrease in the bond angle θ_M and a larger increase in the dihedral angle φ under strain is more

https://doi.org/10.1021/acs.jpclett.5c01362
J. Phys. Chem. Lett. 2025, 16, 5820−5826

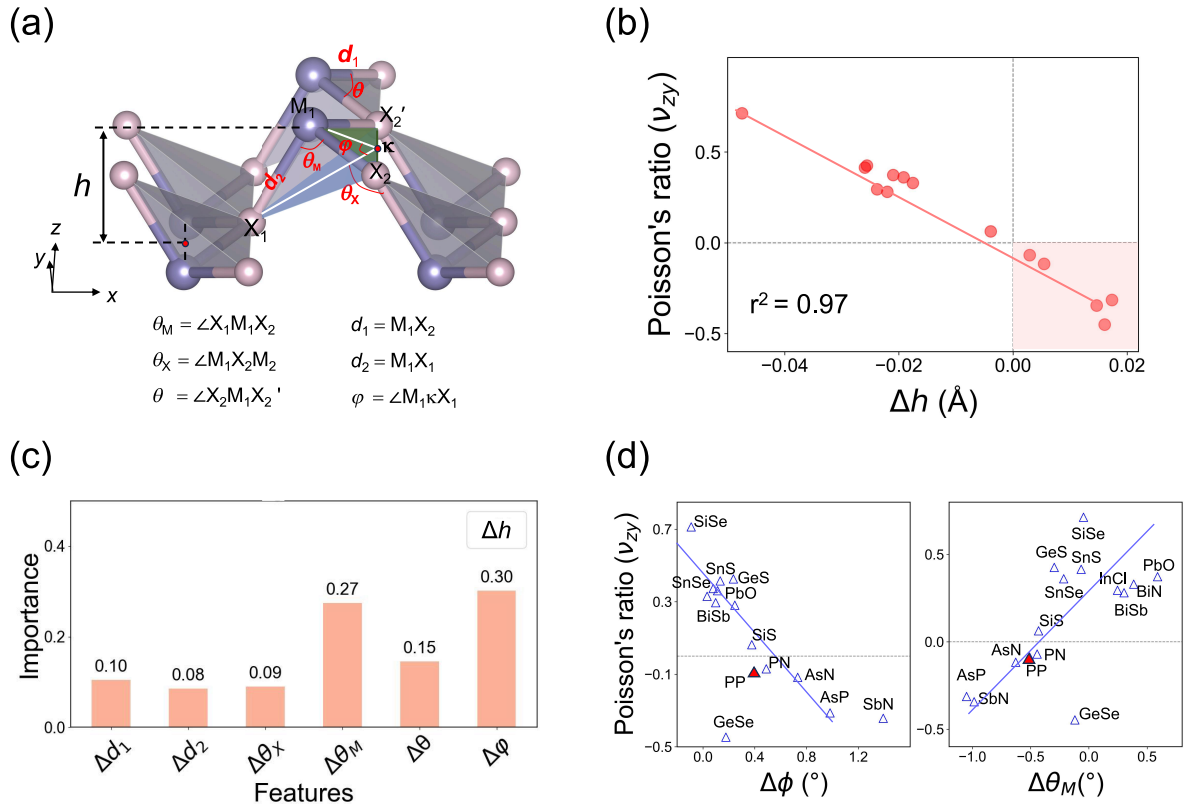

Figure 2. Structural features and machine learning-derived geometric parameter importance for Poisson's ratio. (a) Side view of the geometric structure marked with bond lengths (d_1, d_2), bond angles (θ_M, θ_X, θ), and the dihedral angle (φ). (b) Correlation between Poisson's ratio υ_{zy} and Δh. The pink shaded area in the lower right corner marks the five NPR materials. (c) The influence weights of Δd_1, Δd_2, Δd_1, $\Delta\theta_X$, θ_M, $\Delta\theta$, and $\Delta\varphi$ on Δh. (d) Relationship between υ_{zy} and $\Delta\varphi$ (left panel) and that between υ_{zy} and $\Delta\theta_M$ (right panel), respectively. Black phosphorus (PP), an NPR material, is included for validation and marked by the red-filled triangles.

favorable for the formation of the negative Poisson's ratio. A schematic diagram (Figure S7) is presented to illustrate the movement directions of M and X atoms in NPR materials under *y*-axis strain. The visualization helps to elucidate how the atomic movements of M and X atoms collectively contribute to the NPR responses observed in the material. To validate the identified trends, black phosphorus (PP) is included as an additional data point (the red-filled triangles in Figure 2(d)), which falls along the linear correlations between $\Delta\varphi$ and the Poisson's ratio, as well as between $\Delta\theta_M$ and the Poisson's ratio. However, while the Poisson's ratio generally exhibits a linear correlation with the variations in angles θ_M and φ, GeSe deviates from this trend. Kong et al. previously proposed that the outermost atomic layer of the Se atom is key to the NPR formation in GeSe compared to other family members with M atoms in the outermost layer.[43]

Electronic Structure Effects on Poisson's Ratio. To gain deeper insights into the impact of the electronic structure on NPR formation, we evaluated the orbital contributions of cations and anions in the MX materials. By integrating the projected density of states (PDOS) from $E_f - 0.5$ eV to E_f, we determined the electron occupancy ratios of each orbital for both M and X atoms. Specifically, we calculated the ratio of electrons in the p_z orbital to the total number of electrons in the M atom as the electron occupancy ratio (M_p_z). The ratios are given in the first column of Table S3. Similarly, we obtained the electron occupancy ratios for the X atoms. All of the results are summarized in Table S3, and those for the NPR materials are illustrated in Figure 3(a). It is found that in the NPR materials, including PN, AsN, AsP, and SbN, the electronic states near the Fermi level originate predominantly from the p_z orbitals of both the M and X atoms. In contrast, for positive PR materials, both the p_z and other orbitals contribute to the electronic states near the Fermi level. The distinction suggests that p_z orbital hybridization plays a critical role in the electronic structure of NPR materials, potentially explaining their unique mechanical properties.

To investigate the role of the orbital contribution in the chemical bonding of the NPR materials, we analyzed the bonding characteristics by analyzing the crystal orbital Hamiltonian population (COHP). Figure 3(b) presents the −COHPs for two inequivalent bonds (M_1−X_1 and M_1−X_2) in the MX material system. The results show that the M_1−X_2 bonds have stronger peak intensities than the M_1−X_1 bonds in all NPR materials and exhibit antibonding interactions. Therefore, the M_1−X_2 bond dominates the bonding in the NPR materials. Moreover, the blue shaded region in Figure 3(b) indicates that the antibonding state in M_1−X_2 close to the Fermi level is mainly attributed to the interaction between the p_z orbitals of M_1 and X_2. Figures S9−S12 depict the orbital-resolved interactions (s, p_x, p_y, and p_z) between M_1 and X_2 atoms near the Fermi level, with main contributions from p_z orbitals highlighted using red stars. The results indicate that the bonding between M_1 and X_2 atoms is predominantly driven by the interaction between their p_z orbitals, while the contributions from the s and in-plane p orbitals are comparatively minor.

https://doi.org/10.1021/acs.jpclett.5c01362
J. Phys. Chem. Lett. 2025, 16, 5820−5826

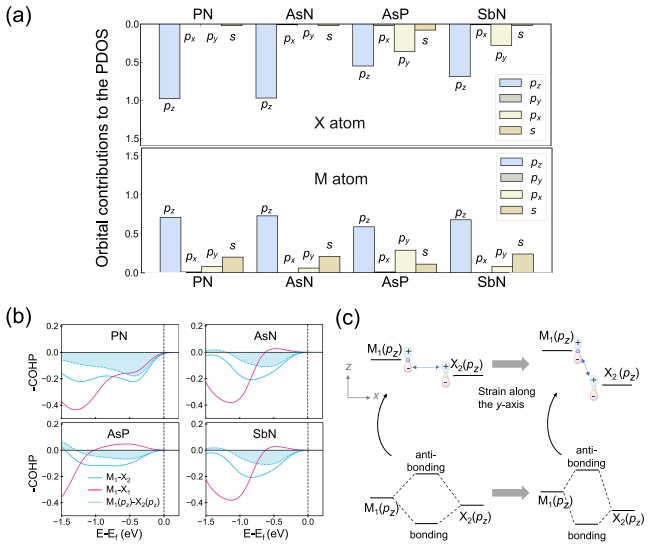

Figure 3. Electronic structures of the NPR materials and the strain-driven mechanism of NPR formation. (a) Orbital contributions to the PDOS on M and X atoms are close to the Fermi-level in the NPR (PN, AsN, AsP, and SbN) materials within the energy range from E_f − 0.5 eV to E_f. The upper panel shows the orbital contributions from X atoms, while the lower panel shows those from M atoms. (b) Crystal Orbital Hamiltonian Population (COHP) for the two inequivalent bonds (M_1−X_1 and M_1−X_2) in the NPR materials. −COHP means the bonding interactions between the atomic orbitals. The pink and blue solid lines correspond to the M_1−X_1 and M_1−X_2 bonds, respectively. The blue shaded region indicates the COHP interaction between the $M_1(p_z)$ orbital and the $X_2(p_z)$ orbital. (c) Interaction between the M_1 (p_z) and X_2 (p_z) orbitals under strain along the zigzag direction drives NPR formation.

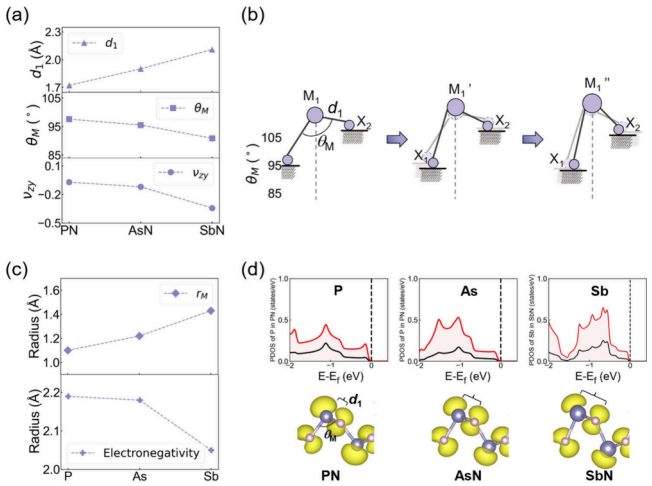

Figure 4. Correlation between the elemental composition, structural parameters, and NPR values. (a) The υ_{zy}, bond length d_1, and bond angle θ_M of PN, AsN, and SbN. As the atomic number of M increases, the bond length (d_1) increases and the bond angle (θ_M) decreases, while the material exhibits a more negative Poisson's ratio υ_{zy}. (b) Schematic diagram of the element−structural correspondence feature: for the same X, the structure of MX evolves as the atomic number of M increases from M_1 to M_1''. (c) The elemental electronegativity and radius of B, As, and Sb. The electronegativity decreases with the increase of radius. (d) The PDOS for cations (P, As, Sb) in MN materials (upper panel) and the corresponding charge density distribution in the energy range from E_f−2 eV to E_f (lower panel).

Figure 3(c) further reveals the NPR formation mechanism related to the interaction between $M_1(p_z)$ and $X_2(p_z)$. The out-of-plane antibonding character arises from the interference between p_z orbitals with antiparallel phase alignment (visualized by "+" and "−" signs in Figure 3(c)). Under tensile strain along the y-direction, the material contracts in the x-direction, resulting in a decrease in the interatomic distance and an increase in the repulsive interaction. To lower the system energy, the material expands along the z-direction to mitigate the repulsive effect of the p_z−p_z antibonding interaction. The resulting structural response leads to a negative Poisson's ratio. Thus, the out-of-plane antibonding characteristics of the p_z−p_z orbital interaction drive the expansion along the z-direction, ultimately leading to the negative Poisson's ratio behavior. The finding establishes a fundamental link between the electronic structure and mechanical properties of the NPR materials.

Correlation among the NPR Values, Structural Parameters, and Elemental Composition. The structure−property relationship is analyzed by linking the NPR values, structural parameters, and element compositions. As revealed in Figure 4(a), the NPR value is negatively correlated with bond length d_1 and positively correlated with bond angle θ_M, suggesting that longer bonds and smaller angles are conducive to more negative NPR values. Figure 4(b) presents a schematic diagram to track how the structural parameters vary with the elemental compositions. For materials sharing the same anionic element X, the cation element M moves upward as the atomic number increases. The upward movement pulls the neighboring X atoms closer, elongating the bond length d_1 while reducing the bond angle θ_M. A representative example is the MN series (M = P, As, or Sb), where the structural evolution follows PN (shortest d_1, largest θ_M) → AsN → SbN (longest d_1, smallest θ_M). By linking the NPR-structure correlation in Figure 4(a) with the structure−composition trend in Figure 4(b), it follows that within the same X element a higher atomic number of M leads to a more negative NPR.

The above mechanism is further explored by examining the variation of the electronegativity and the lone-pair electron cloud distribution. Figure 4(c) shows that the atomic radius increases, while the electronegativity decreases as M changes from P to As and then to Sb. The decrease in electronegativity weakens the electron affinity, thereby reducing M−X bonding interactions. Figure 4(d) shows the PDOS of M (P, As, and Sb) atoms in MN materials, where the DOS peaks for s and p orbitals exhibit clear overlaps. The lower panels show the corresponding charge density distribution in the energy range from E_f − 2 eV to E_f. As M changes from P to Sb, the lone-pair electron cloud distributions on M and X get far away from each other, reducing the repulsion interaction between M and X. The dual effects of decreasing electronegativity and expanding the lone-pair electron cloud distribution drive structural distortion including bond angle (θ_M) contraction and bond length (d_1) elongation. As the bond length increases and the M-X bonding becomes weaker, the material will have a more pronounced response to external strain. Consequently, the change in bond angle ($\Delta\theta_M$) before and after the strain application is more significant. Notably, the larger $\Delta\theta_M$ correlates with the machine-learning based results in Figure 2(d), where a more negative $\Delta\theta_M$ corresponds to a more negative PR ratio. Overall, for NPR materials, changes in atomic number lead to alterations in the electronic and geometric structure, ultimately modulating the Poisson' s ratio.

https://doi.org/10.1021/acs.jpclett.5c01362
J. Phys. Chem. Lett. 2025, 16, 5820−5826

In conclusion, using DFT calculations, we identified five out-of-plane NPR (under y-axis strain) materials from 26 black phosphorene-like candidates with 10 valence electrons: PN, AsN, SbN, AsP, and GeSe. A machine learning model demonstrates that the variations in the bond angle and dihedral angle strongly influence the NPR. The out-of-plane NPR under the y-axis strain is attributed to the interaction between the p_z orbitals of M and X atoms. Furthermore, within NPR materials featuring the same anion element X, a higher atomic number of M corresponds to a more negative Poisson's ratio. These findings provide valuable insights for understanding the NPR formation mechanism of 2D materials, offering a foundation for future research in advanced material design and applications in flexible electronics and strain-engineered devices.

Density functional theory calculations were performed using the Vienna ab initio simulation package,[44−46] employing the Perdew−Burke−Ernzerhof (PBE) functional within the generalized gradient approximation.[47] The MX materials contain two cation atoms and two anion atoms per primitive cell with a Pmn21 space group. The vacuum length for the system is larger than 15 Å in the z-direction to avoid the interaction between neighboring layers. The energy cutoff for the plane-wave basis set is 750 eV. An 18 × 18 × 1 Γ-centered k-point set is utilized for sampling the Brillouin zone. All DFT calculations were performed until the energy and forces on the ions less than 10^{-7} eV and 0.001 eV $Å^{-1}$, respectively.

The Poisson's ratios were obtained by linearly fitting the ε_i and ε_j using the following equation:

$$\varepsilon_i = -\upsilon_{ji}\varepsilon_j \qquad (i, j = x, y, z)$$

where υ_{ji} is the Poisson's ratio and ε_i is the applied strain along the i-direction, while ε_j is the resultant longitudinal strain along the j-direction, respectively.

The key factors influencing Poisson's ratio are identified by a Random Forest machine learning model. The data set comprises five features: variations in two bond lengths and variations in three bond angles. The data set is divided into training and testing sets in a 4:1 ratio. The training results are evaluated through the linear correlation between the predicted and calculated values.

■ ASSOCIATED CONTENT

Supporting Information

The Supporting Information is available free of charge at https://pubs.acs.org/doi/10.1021/acs.jpclett.5c01362.

Calculation result details, including Poisson's ratio value (Table S1) and orbital contribution ratios for M and X atoms (Table S3); fitting curves of the value of Poisson's ratio (Figures S1−S2); effect of SOC on lattice constants (Figure S3); fitting curves of the value of Poisson's ratio considering spin−orbit coupling (Figure S4); mathematical derivation about h (Figure S5); Δh from DFT calculation versus Δh from machine learning prediction (Figure S6); schematic of the moving direction of M and X atoms in monolayer MX under the y-axis strain (Figure S7); projected density of states (Figure S8); and COHP for M_1−X_2 bonds in NPR materials (Figures S9−S12) (PDF)

■ AUTHOR INFORMATION

Corresponding Authors

Yan-Fang Zhang − *School of Physics, University of Chinese Academy of Sciences, Beijing 100049, China*; Email: zhangyanfang@ucas.ac.cn

Shixuan Du − *Beijing National Laboratory for Condensed Matter Physics, Institute of Physics, Chinese Academy of Sciences, Beijing 100190, China; School of Physics, University of Chinese Academy of Sciences, Beijing 100049, China; Songshan Lake Material Laboratory, Dongguan, Guangdong 523808, China;* orcid.org/0000-0001-9323-1307; Email: sxdu@iphy.ac.cn

Authors

Yahong Pu − *Beijing National Laboratory for Condensed Matter Physics, Institute of Physics, Chinese Academy of Sciences, Beijing 100190, China; School of Physics, University of Chinese Academy of Sciences, Beijing 100049, China*

Jie Zhang − *College of Materials Science and Optoelectronic Technology, University of Chinese Academy of Sciences, Beijing 100049, China*

Peixuan Li − *Beijing National Laboratory for Condensed Matter Physics, Institute of Physics, Chinese Academy of Sciences, Beijing 100190, China; School of Physics, University of Chinese Academy of Sciences, Beijing 100049, China*

Guolin Wan − *Beijing National Laboratory for Condensed Matter Physics, Institute of Physics, Chinese Academy of Sciences, Beijing 100190, China; School of Physics, University of Chinese Academy of Sciences, Beijing 100049, China*

Jinbo Pan − *Beijing National Laboratory for Condensed Matter Physics, Institute of Physics, Chinese Academy of Sciences, Beijing 100190, China; School of Physics, University of Chinese Academy of Sciences, Beijing 100049, China;* orcid.org/0000-0003-2612-8232

Complete contact information is available at: https://pubs.acs.org/10.1021/acs.jpclett.5c01362

Author Contributions

S.D. and Y.Z. conceived and supervised the research project. Y.P. performed the first-principles calculations and data analysis. Y.P. wrote the initial manuscript. All authors participated in discussing and editing the manuscripts.

Notes

The authors declare no competing financial interest.

■ ACKNOWLEDGMENTS

This work was supported by funds from the National Key Research and Development Program of China (2022YFA1204100, 2024YFA1207803) and the National Natural Science Foundation of China (52102193, 61888102).

■ REFERENCES

(1) Evans, K. E.; Nkansah, M.; Hutchinson, I.; Rogers, S. Molecular Network Design. *Nature* **1991**, *353* (6340), 124.

(2) Lakes, R. Foam Structures with a Negative Poisson's Ratio. *Science* **1987**, *235* (4792), 1038−1040.

(3) Choi, J. B.; Lakes, R. S. Fracture Toughness of Re-entrant Foam Materials with a Negative Poisson's ratio: Experiment and Analysis. *Int. J. Fract.* **1996**, *80* (1), 73−83.

(4) Fu, M. H.; Zheng, B. B.; Li, W. H. A Novel Chiral Three-dimensional Material with Negative Poisson's Ratio and the Equivalent Elastic Parameters. *Compos. Struct.* **2017**, *176*, 442−448.

(5) Wang, X. T.; Wang, B.; Wen, Z. H.; Ma, L. Fabrication and Mechanical Properties of CFRP Composite Three-dimensional Double-arrow-head Auxetic Structures. *Compos. Sci. Technol.* **2018**, *164*, 92−102.
(6) Choi, J. B.; Lakes, R. S. Nonlinear Properties of Polymer Cellular Materials with a Negative Poisson's Ratio. *J. Mater. Sci.* **1992**, *27* (17), 4678−4684.
(7) Etemadi, E.; Gholikord, M.; Zeeshan, M.; Hu, H. Improved Mechanical Characteristics of New Auxetic Structures Based on Stretch-dominated-mechanism Deformation under Compressive and Tensile Loadings. *Thin-Walled Struct.* **2023**, *184*, No. 110491.
(8) Gao, Y.; Wu, Q. Q.; Wei, X. Y.; Zhou, Z. G.; Xiong, J. Composite Tree-like Re-entrant Structure with High Stiffness and Controllable Elastic Anisotropy. *Int. J. Solids Struct.* **2020**, *206*, 170−182.
(9) Gao, Y.; Zhou, Z. G.; Hu, H.; Xiong, J. New Concept of Carbon Fiber Reinforced Composite 3D Auxetic Lattice Structures Based on Stretching-dominated Cells. *Mech. Mater.* **2021**, *152*, No. 103661.
(10) Sebaq, M.; Liu, Z. Energy Absorption and Vibration Mitigation Performances of Novel 2D Auxetic Metamaterials. *Int. J. Comput. Mater. Sci. Eng.* **2024**, *13* (02), No. 2350022.
(11) Chen, Z. Y.; Wang, Z.; Zhou, S. W.; Shao, J. W.; Wu, X. Novel Negative Poisson's Ratio Lattice Structures with Enhanced Stiffness and Energy Absorption Capacity. *Materials* **2018**, *11* (7), 1095.
(12) Qin, S. A.; Deng, X. L.; Yang, F. M.; Lu, Q. Energy Absorption Characteristics and Negative Poisson's Ratio Effect of Axisymmetric Tetrachiral Honeycombs under In-plane Impact. *Compos. Struct.* **2023**, *323*, No. 117493.
(13) Oh, J. H.; Kim, J. S.; Nguyen, V. H.; Oh, I. K. Auxetic Graphene Oxide-porous Foam for Acoustic Wave and Shock Energy Dissipation. *Compos. Part. B Eng.* **2020**, *186*, No. 107817.
(14) Cheng, X.; Zhang, Y.; Ren, X.; Han, D.; Jiang, W.; Zhang, X. G.; Luo, H. C.; Xie, Y. M. Design and Mechanical Characteristics of Auxetic Metamaterial with Tunable Stiffness. *Int. J. Mech. Sci.* **2022**, *223*, No. 107286.
(15) Li, Z. Y.; Gao, W.; Wang, M. Y.; Wang, C. H.; Luo, Z. Three-dimensional Metamaterials Exhibiting Extreme Isotropy and Negative Poisson's Ratio. *Int. J. Mech. Sci.* **2023**, *259*, No. 108617.
(16) Cui, J.; Zhang, L.; Gain, A. K. A Novel Auxetic Unit Cell for 3D Metamaterials of Designated Negative Poisson's Ratio. *Int. J. Mech. Sci.* **2023**, *260*, No. 108614.
(17) Montazeri, A.; Bahmanpour, E.; Safarabadi, M. A Poisson's Ratio Sign-switching Mechanical Metamaterial with Tunable Stiffness. *Int. J. Mech. Sci.* **2023**, *260*, No. 108670.
(18) Wang, Y.; Li, F.; Li, Y. F.; Chen, Z. F. Semi-metallic Be_5C_2 Monolayer Global Minimum with Quasi-planar Pentacoordinate Carbons and Negative Poisson's Ratio. *Nat. Commun.* **2016**, *7* (1), No. 11488.
(19) Qian, S.; Sheng, X.; Zhou, Y.; Yan, X.; Chen, Y.; Huang, Y.; Huang, X.; Feng, E.; Huang, W. Two-dimensional Be_2C with Octacoordinate Carbons and Negative Poisson's Ratio. *J. Phys. Chem. C* **2018**, *122* (14), 7959−7967.
(20) Li, X.; Gao, L. B.; Zhou, W. Z.; Wang, Y. J.; Lu, Y. Novel 2D Metamaterials with Negative Poisson's Ratio and Negative Thermal Expansion. *Extreme Mech. Lett.* **2019**, *30*, No. 100498.
(21) Qin, G. Z.; Qin, Z. Z. Negative Poisson's Ratio in Two-dimensional Honeycomb Structures. *npj Comput. Mater.* **2020**, *6* (1), 51.
(22) Ma, Z.; Huang, P.; Li, J.; Zhang, P.; Zheng, J. X.; Xiong, W.; Wang, F.; Zhang, X. W. Multiferroicity and Giant In-plane Negative Poisson's Ratio in Wurtzite Monolayers. *npj Comput. Mater.* **2022**, *8* (1), 51.
(23) Yu, L.; Wang, Y.; Zheng, X.; Wang, H.; Qin, Z.; Qin, G. Emerging Negative Poisson's Ratio Driven by Strong Intralayer Interaction Response in Rectangular Transition Metal Chalcogenides. *Appl. Surf. Sci.* **2023**, *610*, No. 155478.
(24) Peng, R.; Ma, Y. D.; He, Z. L.; Huang, B. B.; Kou, L. Z.; Dai, Y. Single-Layer AgS: A Two-dimensional Bidirectional Auxetic Semiconductor. *Nano Lett.* **2019**, *19* (8), 5827−5833.
(25) Jin, W. Y.; Sun, W. G.; Kuang, X. Y.; Lu, C.; Kou, L. Z. Negative Poisson Ratio in Two-dimensional Tungsten Nitride: Synergistic Effect from Electronic and Structural Properties. *J. Phys. Chem. Lett.* **2020**, *11* (22), 9643−9648.
(26) Hu, Q.; Lu, G.; Tse, K. M. Compressive and Tensile Behaviours of 3D Hybrid Auxetic-honeycomb Lattice Structures. *Int. J. Mech. Sci.* **2024**, *263*, No. 108767.
(27) Xiong, W.; Huang, K.; Yuan, S. The Mechanical, Electronic and Optical Properties of Two-dimensional Transition Metal Chalcogenides MX_2 and M_2X_3 (M= Ni, Pd; X= S, Se, Te) with Hexagonal and Orthorhombic Structures. *J. Mater. Chem. C* **2019**, *7* (43), 13518−13525.
(28) Ma, F. X.; Jiao, Y. L.; Wu, W. K.; Liu, Y.; Yang, S. Y. A.; Heine, T. Half-auxeticity and Anisotropic Transport in Pd Decorated Two-dimensional Boron Sheets. *Nano Lett.* **2021**, *21* (6), 2356−2362.
(29) Zhu, Y. C.; Cao, X. F.; Tan, Y.; Wang, Y.; Hu, J.; Li, B. T.; Chen, Z. Single-layer MoS_2: A Two-dimensional Material with Negative Poisson's Ratio. *Coatings* **2023**, *13* (2), 283.
(30) Jiang, J. W.; Park, H. S. Negative Poisson's Ratio in Single-layer Graphene Ribbons. *Nano Lett.* **2016**, *16* (4), 2657−2662.
(31) Zhu, Y. L.; Qu, Z. H.; Zhang, J. S.; Wang, X. T.; Jiang, S.; Xu, Z. Y.; Yang, F.; Wu, Z. H.; Dai, Y. H. First-principles Prediction of Ferroelectric Janus SiXY (X/Y = S/Se/Te, X ≠ Y) Monolayers with Negative Poisson's Ratios. *Phys. Chem. Chem. Phys.* **2024**, *26* (5), 4555−4563.
(32) Zhang, G. T.; Chen, Q.; Wang, J. L. Structural Phase Transition and Electronic Properties of Two-dimensional $NbOI_2$. *Phys. Rev. B* **2024**, *109* (18), No. 184103.
(33) Mustahsan, F.; Khan, S. Z.; Zaidi, A. A.; Alahmadi, Y. H.; Mahmoud, E. R. I.; Almohamadi, H. Re-entrant Honeycomb Auxetic Structure with Enhanced Directional Properties. *Materials* **2022**, *15* (22), 8022.
(34) Li, F. Y.; Zhang, Q.; Wang, Z. J.; Zhu, D. C. A New Three-dimensional Re-entrant Negative Poisson's Ratio Metamaterial with Tunable Stiffness. *Eng. Struct.* **2024**, *306*, No. 117793.
(35) Valle, R.; Pincheira, G.; Tuninetti, V. Design of an Auxetic Cellular Structure with Different Elastic Properties in Its Three Orthogonal Directions. *P. I. Mech. Eng. I-J. Mater.* **2021**, *235* (6), 1341−1350.
(36) Jiang, J. W.; Park, H. S. Negative Poisson's Ratio in Single-layer Black Phosphorus. *Nat. Commun.* **2014**, *5*, 4727.
(37) Wang, H. D.; Li, X. X.; Sun, J. Y.; Liu, Z.; Yang, J. L. BP_5 Monolayer with Multiferroicity and Negative Poisson's Ratio: A Prediction by Global Optimization Method. *2d Mater.* **2017**, *4* (4), No. 045020.
(38) Lang, J. P.; Han, D.; Zhang, X. G.; Jiang, W.; Zhang, Y.; Ni, X.h.; Hao, J.; Teng, X. C.; Ren, X. A Star-shaped Tubular Structure with Multiple-directional Auxetic Effect. *Thin-Walled Struct.* **2023**, *193*, No. 111247.
(39) Yu, L. P.; Yan, Q. M.; Ruzsinszky, A. Negative Poisson's Ratio in 1T-type Crystalline Two-dimensional Transition Metal Dichalcogenides. *Nat. Commun.* **2017**, *8*, No. 15224.
(40) Pan, J. B.; Zhang, Y. F.; Zhang, J. D.; Banjade, H.; Yu, J.; Yu, L. P.; Du, S. X.; Ruzsinszky, A.; Hu, Z. P.; Yan, Q. M. Auxetic Two-dimensional Transition Metal Selenides and Halides. *npj Comput. Mater.* **2020**, *6* (1), 154.
(41) Gao, W. J.; Shi, X. B.; Qiao, Y. S.; Yu, M. Y.; Yin, H. B. Strain-dependent Near-zero and Negative Poisson Ratios in a Two-dimensional $(CuI)P_4SSe_4$ Monolayer. *Phys. Rev. B* **2024**, *109* (7), No. 075402.
(42) Mao, Y. Q.; Zhang, J. Y.; Bai, S. L.; Wu, M. X.; Luo, D. M.; Tang, S. W. The Electronic, Mechanical Properties and In-plane Negative Poisson's Ratio in Novel Pentagonal NiX_2 (X = S, Se, Te) Monolayers with Strong Anisotropy: A First-principles Prediction. *Comput. Mater. Sci.* **2023**, *216*, No. 111873.
(43) Kong, X.; Deng, J. K.; Li, L.; Liu, Y. L.; Ding, X. D.; Sun, J.; Liu, J. Z. Tunable Auxetic Properties in Group-IV Monochalcogenide Monolayers. *Phys. Rev. B* **2018**, *98* (18), No. 184104.

https://doi.org/10.1021/acs.jpclett.5c01362
J. Phys. Chem. Lett. 2025, 16, 5820−5826

(44) Kresse, G.; Furthmuller, J. Efficient Iterative Schemes for Ab Initio Total-energy Calculations Using a Plane-wave Basis Set. *Phys. Rev. B* **1996**, *54* (16), 11169−11186.
(45) Kresse, G.; Furthmuller, J. Efficiency of Ab-initio Total Energy Calculations for Metals and Semiconductors Using a Plane-wave Basis Set. *Comput. Mater. Sci.* **1996**, *6* (1), 15−50.
(46) Kresse, G. Ab-initio Molecular-dynamics for Liquid-metals. *J. Non-Cryst. Solids.* **1995**, *193*, 222−229.
(47) Perdew, J. P.; Burke, K.; Ernzerhof, M. Generalized Gradient Approximation Made Simple. *Phys. Rev. Lett.* **1996**, *77* (18), 3865−3868.

https://doi.org/10.1021/acs.jpclett.5c01362
J. Phys. Chem. Lett. 2025, 16, 5820−5826